energies

MDPI

Article

Direct Visualization of Nanoscale Salt Precipitation and Dissolution Dynamics during CO_2 Injection

Xinling Hu [1], Jian Wang [1], Liang Zhang [1], Hongli Xiong [1], Zengding Wang [2], Huazheng Duan [2], Jun Yao [2], Hai Sun [2], Lei Zhang [2], Wenhui Song [2] and Junjie Zhong [2,*]

[1] Exploration and Development Research Institute Sinopec Jianghan Oilfield Company, Wuhan 430223, China
[2] Research Center of Multiphase Flow in Porous Media, School of Petroleum Engineering, China University of Petroleum (East China), Qingdao 266580, China
* Correspondence: zhongjunjie@upc.edu.cn

Abstract: CO_2 injection to enhance shale oil recovery provides a win-win solution to meet the global fuel shortage and realize ultimate carbon neutrality. When shale reservoirs contain high salinity water, CO_2 injection can result in salt precipitation to block the nanometer pores in the shale, causing undesirable formation damage. Understanding salt precipitation and dissolution dynamics at the nanoscale are fundamental to solving this practical challenge. In this work, we developed a shale micromodel to characterize salt precipitation and dissolution based on nanofluidic technology. By directly distinguishing different phases from 50 nm to 5 μm, we identified the salt precipitation sites and precipitation dynamics during the CO_2 injection. For the salt precipitation in the nanometer network, we identified two precipitation stages. The ratio of the precipitation rates for the two stages is ~7.9 times that measured in microporous media, because of the slow water evaporation at the nanoscale. For the salt precipitation in the interconnected micrometer pores, we found that the CO_2 displacement front serves as the salt particle accumulating site. The accumulated salt particles will in turn impede the CO_2 flow. In addition, we also studied the salt dissolution process in the shale micromodel during water injection and found the classical dissolution theory overestimates the dissolution rate by approximately twofold. This work provides valuable pore-scale experimental insight into the salt precipitation and dissolution dynamics involved in shale formation, with the aim to promote the application of CO_2 injection for shale oil recovery.

Keywords: CCUS; CO_2 injection; shale oil; microfluidics; salt precipitation

Citation: Hu, X.; Wang, J.; Zhang, L.; Xiong, H.; Wang, Z.; Duan, H.; Yao, J.; Sun, H.; Zhang, L.; Song, W.; et al. Direct Visualization of Nanoscale Salt Precipitation and Dissolution Dynamics during CO_2 Injection. *Energies* **2022**, *15*, 9567. https://doi.org/10.3390/en15249567

Academic Editor: Mofazzal Hossain

Received: 17 November 2022
Accepted: 13 December 2022
Published: 16 December 2022

1. Introduction

The CO_2 injection is a promising innovation to rejuvenate shale oil reservoirs after primary production [1–3]. Given the nanometer pore sizes and ultra-low permeabilities (down to nano-Darcy) of shale reservoirs [4,5], CO_2 is able to improve the oil recovery efficacy by its excellent mixability with oil, leading to oil swelling and oil viscosity reduction [6,7]. However, when the formation rocks consist of a large proportion of halite, the shale formation water often contains high salinity, especially after hydraulic fracturing with massive water injected [8]. A typical example of this type of shale reservoir is the one discovered in the Qianjiang depression of the Jianghan basin in China, which is characterized by its multiple rhythmic layers of salt rock and gypsum [9]. Injecting CO_2 into the shale oil reservoir with high salinity water could result in salt precipitation blocking the nanometer flow pathway in shale, resulting in undesirable formation damage similar to asphaltene precipitation [10].

The salt precipitation in the porous media during CO_2 injection has been widely studied for carbon sequestration and storage in saline aquifers [11,12]. The saline aquifer is featured by its large pore sizes (at 10^1–10^2 μm) [13] and high permeability (at 10^2–10^3 mD) [14]. By using core-flooding with CT scanning, previous studies have pointed out that salt precipitation in the saline aquifer can reduce formation permeability by up to three orders of

magnitude [15–17]. Two types of salt precipitation in porous media have been identified, including homogeneous and local salt precipitations. The homogeneous salt precipitation is believed to cause minor damage to permeability as the pore size in the saline aquifer is orders of magnitude larger than the size of the deposited salt particles. The local salt precipitation, however, is regarded as the main reason to block the near-wellbore area and leads to obvious permeability reduction [18]. Developing chemicals to minimize salt precipitation is thus vital to protect reservoir permeability [19].

The shale reservoir is highlighted by its ultra-small pore sizes (mainly at 10^0–10^2 nm). Thus, even the homogeneous salt precipitation could lead to significant porosity and permeability reduction [20]. For example, salt precipitation has been recently found to cause up to ~90% permeability reduction in tight formation rocks [21,22]. In addition, the salt precipitation in nanometer pores has also been identified to reduce the mechanical strength of shale [23]. At the nanometer pore scale, salt precipitation dynamics during CO_2 injection remain largely unknown. The core flooding method is limited at the nanoscale to understand the salt precipitation dynamics during CO_2 injection. Even with the help of CT scanning, characterizing salt precipitation in the nanometer pores of shale samples remains challenging. Therefore, finding an alternative approach to provide nanometer pore-scale insight into the salt precipitation in shale reservoirs is crucial.

Microfluidics has been used to characterize pore-scale salt precipitation dynamics of CO_2 injection in saline aquifers [24,25]. At the nanometer pore scale, researchers have recently applied nanofluidics to study fluid fundamentals in shale reservoirs down to the sub-10 nm scale, including hydrocarbon phase transitions [26,27] and fluid transport properties [28,29]. Fluid behaviors in nanometer pores are often found to deviate from bulk fluid properties [28,30]. For the CO_2 injections into shale oil reservoirs, a previous nanofluidic study has identified immiscible and miscible flooding phenomena in a 60-nm network chip, as well as huff-n-puff mechanisms [31]. Salt precipitation dynamics during CO_2 injections at the nanoscale have not yet been studied with nanofluidics, and remain obscure from the experimental perspective. To fill this gap, we fabricated a multiscale (50 nm, 500 nm and 5 μm) nanofluidic porous chip to study salt precipitation during the CO_2 injection. We identified the preferential precipitation scale during the CO_2 injection. With image analysis, we characterized the salt precipitation dynamics in the nanometer network and pores, and found deviations to the salt precipitation dynamics in the micrometer porous media of saline aquifers. In addition, we performed water injection after CO_2 injection to dissolve salt, and identified the dissolution dynamics in the nanometer network deviating from classical dissolution theory. This work aims to provide the nanometer pore-scale insight of salt precipitation during CO_2 injections into shale oil reservoirs, from a fundamental and experimental aspect.

2. Material and Methods

To provide a nanometer pore-scale physical micromodel of the shale reservoir, we fabricated a nanofluidic chip considering three levels of pore features (Figure 1): (i) a 50-nm deep interconnected network (fabricated as 52.7 ± 4.6 nm for the channel depth and 2 μm for the channel width) to simulate the connected nanometer pores in shale matrix; (ii) a 500-nm deep interconnected network (fabricated as 516.1 ± 9.8 nm for the channel depth and 20 μm for the channel width) to simulate the nanometer natural fractures in shale; (iii) 5-μm deep pores (fabricated as 5.1 ± 0.1 μm for the pore depth and approximately 100–300 μm for the equivalent diameter on the chip surface) to simulate large dissolution pores in shale. For all fabricated features, the depth of the feature is the governing dimension for the fluid transport and salt precipitation. The width of the feature provides visibility to distinguish different phases (CO_2, water and salt) under the microscope. The nanoporous media flank two main microchannels to supply testing fluids (salt solution, pure water and CO_2). The width of the entire nanoporous media is 2 mm. To fabricate the nanofluidic chip, we repeated photolithography and reactive ion etching three times. After that, we performed

anodic bonding and chip dicing. The detailed multiscale chip fabrication methods are delineated in our previous work [32,33].

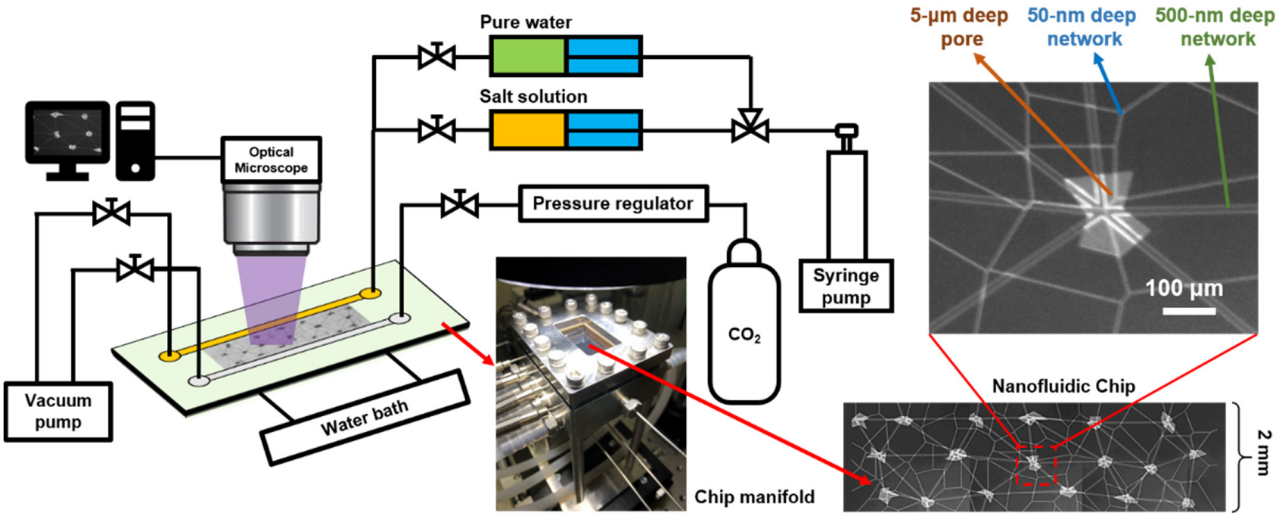

Figure 1. Schematic and photos of the experimental setup and the nanofluidic chip.

The schematic of the experimental setup is shown in Figure 1. The fabricated nanofluidic chip is mounted in a self-manufactured stainless-steel manifold to allow high temperature and pressure tests. The metal manifold is then connected with pistons, syringe pumps and gas cylinders perform the fluid injections. To simulate reservoir temperatures, we connected a water bath to the manifold for circulating hot water, and measured the experimental temperature by inserting thermocouples. In our experiments, the temperature is controlled at 70 $\pm$ 1.2 °C for the entire chip, which is close to the shale reservoir temperature. The experimental results are captured as images by the optical microscope connected with a mounted digital camera.

3. Results and Discussion

To study salt precipitation during the CO_2 injection in the nanoporous media. We first vacuumed the chip for 1 h to remove the air initially in the chip. Then, we injected the mixed salt solution (NaCl = 282.9 g/L, Na_2SO_4 = 10.6 g/L, $CaSO_4$ = 1.6 g/L) into the nanofluidic chip. The composition of salts in the mixed solution is formulated based on the salinity analysis results of the produced water in four wells in the field. After salt solution injection, the CO_2 gas is injected at a constant 1 MPa pressure. The pressure is larger than the maximum capillary pressure in the 50-nm deep network (~0.76 MPa). We defined the moment when the gas bubble is observed in the porous media as $t = 0$ s. The salt precipitation results are then recorded by the camera connected with the optical microscope, as shown in Figure 2.

At the early stage of CO_2 injection (~2 s), gas bubbles are generated in the 5-μm deep pores without noticeable salt precipitation (Figure 2a). With the CO_2 further injection, salt contents start to nucleate in the 500-nm deep network (Figure 2b), and then in the 5-μm deep pores (Figure 2c). The precipitated salt then grows and accumulates at both scales with continuous CO_2 injection. However, the salt solution in the 50-nm deep network remains in the liquid phase for the entire CO_2 injection process (Figure 2d).

3.1. Salt Precipitation Dynamics in the Nanometer Network

To quantify the salt precipitation dynamics in the 500-nm deep network, we performed image analysis to extract the 500-nm network from the original images captured by the microscope camera (Figure 3a). The extracted grayscale image sequence is then calculated in MATLAB to quantify the precipitated salt in the 500-nm network. Three stages of the salt precipitation in the 500-nm deep network are identified (Figure 3b). We defined the

occupancy of the solid salt particles in the 500-nm deep network as a ratio between the total volume of salt particles and the network (Figure 3a). In the first 1.6 s, CO_2 injection leads to negligible salt deposition, and water displacement and evaporation mainly happen at this stage. After the salt concentration reaches saturation, salt precipitates fast in the 500-nm deep network (1.6 to 4.7 s) due to heterogeneous salt nucleation in the solution. After 4.7 s, salt contents precipitate and deposit slowly in the 500-nm deep network due to water evaporation.

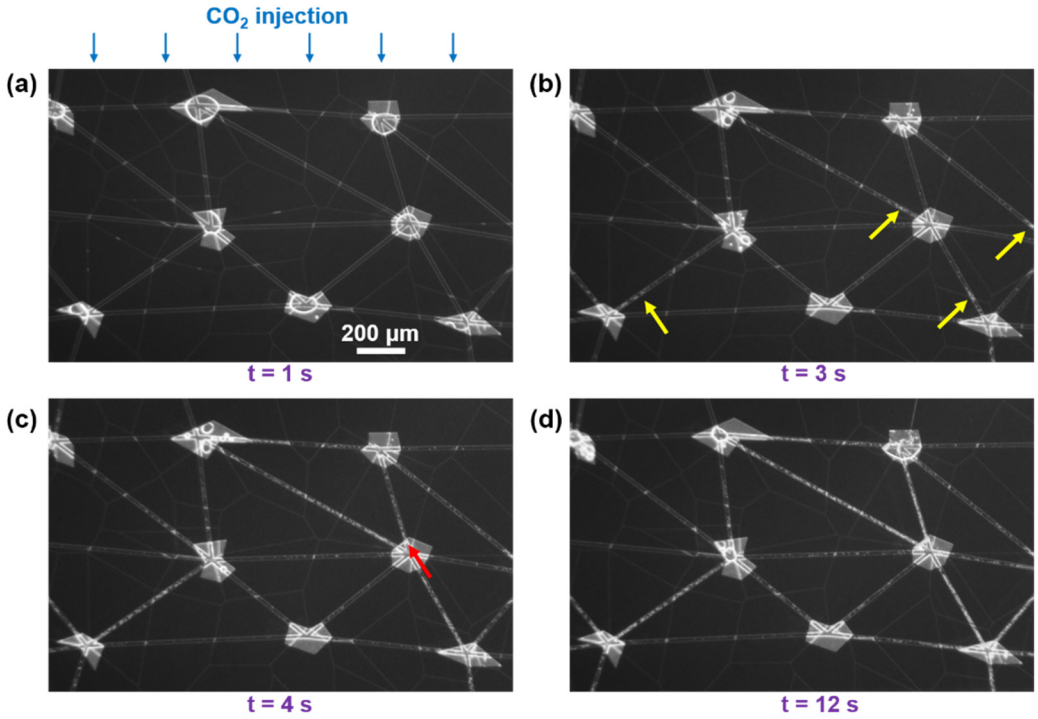

Figure 2. Salt precipitation in the 500-nm deep network and 5-μm deep pores during CO_2 injection at constant pressure (1 MPa). (**a**–**d**) are recorded images of salt precipitation at approximately 1, 3, 4 and 12 s. The white particles are the precipitated salt contents. The yellow and red arrows indicate salt precipitations in the 500-nm deep network and 5-μm deep pores.

We used linear fit to estimate the salt participation rates of the latter two stages. In the fast salt precipitation stage (1.6 to 4.7 s), the occupancy of solid salt particles grows at a fitting rate of 9.1 ± 0.5%/s (R^2 = 0.95) (Figure 3c). In the slow salt precipitation stage (after 4.7 s), the growth rate of the occupancy of solid salt particles is fitted at 0.37 ± 0.02%/s (R^2 = 0.89) (Figure 3d). Therefore, the salt precipitation rate in the fast salt precipitation stage is ~24.6 times of the growth rate in the slow salt precipitation stage. We defined a precipitation rate ratio I to quantify this difference (i.e., $I = 24.6$).

The three stages of the salt precipitation dynamics in porous media have also been detected in a recent microfluidic study to identify CO_2-injection-caused salt precipitation in deep saline aquifers [34] The pore size in the literature is defined by the height of the micropillars to be 25 μm. The salt growth rate in the fast salt precipitation stage is measured to be ~3.1 times that of the slow salt precipitation stage (i.e., precipitation rate ratio $I = 3.3$). The precipitation rate ratio in the microporous media is thus ~7.9 times lower than that measured in our work. A potential reason for the large discrepancy between the two cases is that the water evaporation rate at the nanoscale is much lower than that at the microscale. The previous study indicates that the liquid evaporation rate (v_g) in porous media can be calculated by [33]:

$$v_g = \frac{P_s - P_v}{\frac{R_{kn}R_{vis}}{R_{kn}+R_{vis}} + R_{if}} \quad (1)$$

where P_s is the saturation pressure of the liquid in porous media, P_v is the vapor partial pressure in gas, R_{kn} is the Knudsen flow resistance defined by the Knudsen diffusion [35], R_{vis} is the viscous flow resistance defined by the Darcy's law, R_{if} is the liquid-vapor interfacial resistance defined by the Hertz-Knudsen equation [36]. R_{kn}, R_{vis} and R_{if} for the porous media consisting of slit pores are:

$$R_{kn} = \frac{3\rho_v^{mol}\tau L_v}{4h\varphi}\sqrt{2\pi RTM} \tag{2}$$

$$R_{vis} = \frac{L_v\mu_v}{k_v} \tag{3}$$

$$R_{if} = \frac{\rho_v}{a}\sqrt{\frac{2\pi RT}{M}} \tag{4}$$

where ρ_g^{mol} is the molar density of vapor phase, τ is the tortuosity of the porous media, L_v is the total length of the porous media, h is the height of a slit pore, φ is the porosity of the porous media, R is the gas constant, T is the temperature, M is the molar mass, μ_v is the vapor viscosity, k_v is the permeability of the vapor in porous media, ρ_v is the density of the vapor, a is a constant and in most cases equals 1. When the length of the porous media is orders of magnitude larger than the pore size (e.g., the height of a slit pore), R_{if} becomes negligible [33], and the water evaporation rate is mainly governed by R_{kn} and R_{vis}. The permeability of vapor in a porous media consisting of slit pores can be expressed as:

$$k = \frac{\varphi h^2}{12} \tag{5}$$

Based on Equations (1)–(5), the liquid evaporation rate can be further expressed as:

$$v_g = (P_s - P_v)\left(\frac{\varphi h^2}{12L_v\mu_v} + \frac{4h\varphi}{3\tau\rho_v^{mol}L_v\sqrt{2\pi RTM}}\right) \tag{6}$$

For qualitative comparison, we considered a straight channel (i.e., $\varphi = \tau = 1$) and assumed that the water vapor partial pressure in the gas phase is low ($P_v \approx 0$) when the CO_2 pressure is high. Based on Equation (6), the minimum water evaporation rate in our case ($h = 500$ nm, $L_v = 2$ mm, $T = 343$ K) is calculated to be ~5.5 times slower than the minimum water evaporation rate in the literature ($h = 25$ µm, $L_v \approx 30$ mm, $T = 293$ K) [34]. The difference in evaporation rates (5.5 times) contributes to the difference (7.9 times) in the precipitation rate ratio between the two cases. Therefore, we deduced that in the shale nanoporous media, slow salt precipitation caused by long-term CO_2 injection is less pronounced than that in the deep saline aquifer because of a much lower water evaporation rate.

The precipitated salt from the fast salt precipitation stage contributes more significantly to the total precipitated salt in the nanoporous media than in the microporous media. In our case, we found that 23.9% volume of the 500-nm deep network is occupied by precipitated salt after ~13 s of CO_2 injection. At the fast salt precipitation stage, 20.3% of the network volume is occupied by precipitated salt particles, contributing to ~85% of the total deposited salt. In the literature [34], salt depositing at the fast salt precipitation stage contributes to ~77% of the total precipitated salt. The dynamics of the fast salt precipitation are governed by nucleation. Previous research points out that heterogeneous nucleation has a much lower nucleation energy barrier than homogenous nucleation [37]. In the porous media, the pore surface provides favorable nucleation sites, and heterogeneous nucleation plays a dominant role. As the surface-to-volume ratio scales with L, nanoporous media has a much larger surface-to-volume ratio than microporous media, providing a higher density of nucleation sites for heterogeneous nucleation. Therefore, salt prefers to precipitate early in the shale nanoporous media due to heterogeneous nucleation.

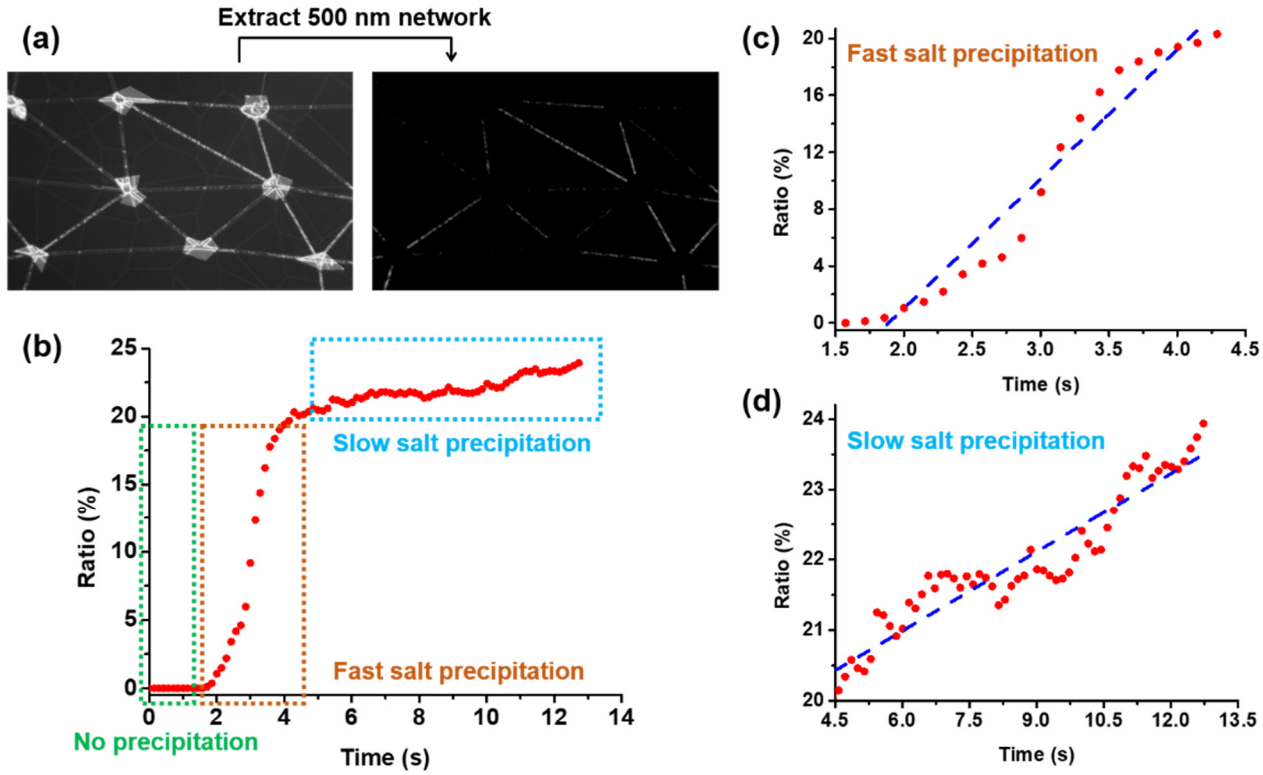

Figure 3. Salt precipitation dynamics in the 500-nm deep network. (**a**) Image analysis to extract precipitated salt particles in the 500-nm deep network. (**b**) the occupancy of the salt particles in the 500-nm deep network. The ratio is defined as the total volume of the precipitated salt divided by the total volume of the 500-nm deep network in the observation area. (**c**) Fast salt precipitation and its linear fitting result (slope = 9.1 ± 0.5, R^2 = 0.95). (**d**) Slow salt precipitation and its linear fitting result (slope = 0.37 ± 0.02, R^2 = 0.89).

During the relatively low-pressure CO_2 injection (1 MPa), we realized that the 50-nm deep network remains liquid-filled even through the gas pressure is larger than the capillary pressure. We injected high-pressure CO_2 (5 MPa) from the opposite main channel to validate the connectivity of the 50-nm deep network and test the potential of salt precipitation at the 50-nm scale. We found the salt solution in the 50-nm deep network is displaced by CO_2 due to a large pressure gradient. During the high-pressure gas injection, we still did not detect salt particles nucleating and growing in the 50-nm deep network. A potential reason is that salt nucleation is unfavorable at the 50-nm scale due to the energy barrier for forming stable nuclei.

The classical nucleation theory [38] provides qualitative insight into the experimental result. In the classical nucleation theory, the free energy change (ΔG) of the nucleus formation includes the free energy change due to the nucleus interface (ΔG_s) and the free energy change due to the nucleus volume (ΔG_v):

$$\Delta G = \Delta G_s + \Delta G_v \tag{7}$$

Here ΔG_s is positive and inhibits the nucleation, as the additional interfacial energy generated by the nucleus is unfavorable in a thermodynamic system. ΔG_v is negative and promotes the nucleation, because ions have lower chemical potential in the precipitated salts (μ_n) compared to in solution (μ_s) at supersaturation. Equation (7) can be further derived as a function of the nucleus radius (r):

$$\Delta G = 4\pi r^2\gamma - \frac{4\pi r^3}{3V_m}(\mu_s - \mu_n) \tag{8}$$

Here γ is the interfacial tension between nucleus and solution, V_m is the volume of the unit cell in a bulk salt crystal. The schematic of the free energy of the nucleus changing with nucleus radius is shown in Figure 4. A free energy change barrier (ΔG_{max}) exists for nucleation, and the corresponding nucleus radius is the critical nucleus radius (r_c):

$$r_c = \frac{2\gamma V_m}{\mu_s - \mu_n} \tag{9}$$

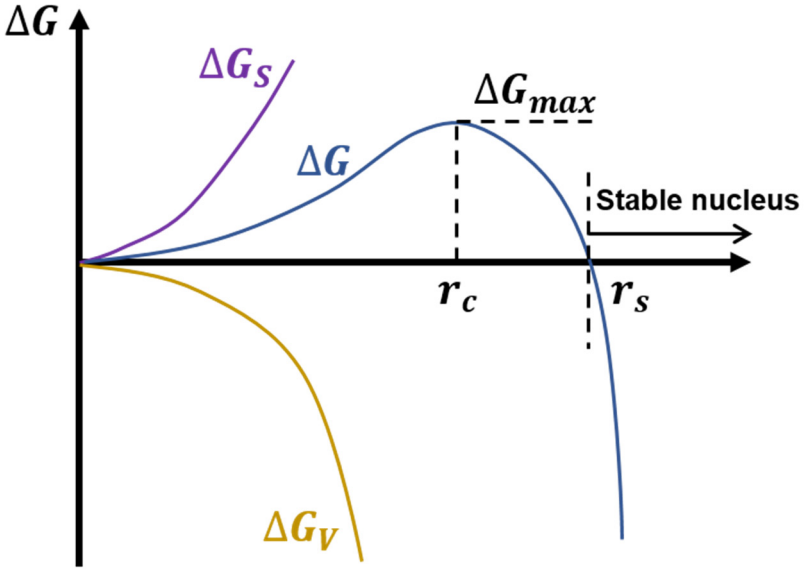

Figure 4. Schematic of the free energy change of a growing nucleus.

When the radius of the initially precipitated salt nucleus is smaller than r_c, the nucleus will not grow into a salt crystal. In addition, the free energy change needs to be negative ($\Delta G < 0$) for the growth of the nucleus to be thermodynamically favorable. Therefore, the minimum stable nucleus radius (r_s) is determined by $\Delta G = 0$:

$$r_s = \frac{3\gamma V_m}{\mu_s - \mu_n} \tag{10}$$

The critical nucleus radius changes with the composition, concentration and supersaturation conditions [39]. As we used a mixed salt solution in our experiments, determining the accurate salt nucleus size is challenging. The main composition of the simulated formation water is sodium chloride. The concentration of sodium chloride is close to saturation. Therefore, we can use the critical nucleus radius of sodium chloride as a reference. In a previous experimental study, aqueous sodium chloride was introduced to carbon nanotubes, and real-time electron microscopy at atomic resolution was used to detect the sodium chloride nucleation and precipitation [40]. The size of a stable sodium chloride nucleus is found to be on the order of several nanometers. Compared to the 500-nm deep network, the 50-nm deep network is only one order of magnitude larger than the stable sodium chloride nucleus size. The salt nucleus, once formed under perturbation, is less likely to be large and stable in the 50-nm deep network compared to the 500-nm deep network due to the confinement effect.

Another potential reason for the salt not precipitating in the 50-nm deep network during high-pressure CO_2 injection is that the salt solution was displaced by CO_2 before water evaporated to allow salt nucleation. We estimated that the minimum water evaporation rate in the 500-nm deep network is ~14.7 times faster than that in the 50-nm deep network from Equation (6). Since the CO_2 displacing salt solution happened within a similar time-lapse (~10 s) in both cases, the slow evaporation rate in the 50-nm deep network results in the salt solution being displaced by CO_2 before any nucleation could ever happen. In general,

we believed that salt precipitation is unfavorable in the relatively small nanometer pores in shale matrix because the minimum stable nucleus size approaches the confinement size, and a large pressure gradient is needed to overcome the capillarity and flow resistance during CO_2 injection.

3.2. Salt Precipitation in the Micrometer Pores Connected by Nanometer Throats

During the CO_2 injection at 1 MPa, we found that salt also precipitates at the connection between the 500-nm deep network and 5-μm deep pores (Figure 5a). The precipitated salt accumulates at the inlet of the pores. We performed image analysis to evaluate the salt accumulation in three individual pores with 1, 2 and 3 inlets (Figure 5b). The three pores (Pore1, 2 and 3, Figure 5a) are ~0.35, 1 and 1.74 mm from the CO_2 injection main channel, respectively. During the CO_2 injection, the salt particles do not accumulate in the pore for the first 2.7 s, which is 1.1 s later than the initiation of salt precipitation in the 500-nm deep network. After that, the salt particles accumulate at a similar rate in all three pores, and occupy a sector area at each inlet. The fast salt precipitation in the pore ends earlier when the pore is closer to the CO_2 injection main channel (Pore1 at 5.2 s, Pore2 at 6.1 s and Pore3 at 7.7 s, Figure 5b). Meanwhile, the area that salt particles occupy per inlet is smaller when the pore is closer to the CO_2 injection main channel (Pore1 at 514 μm^2, Pore2 at 556 μm^2 and Pore3 at 638 μm^2, Figure 5b). From the experimental results, we deduced that the pore endures a larger CO_2 pressure drop when the pore is closer to the CO_2 injection main channel. The CO_2 displaces salt solution faster in pores closer to the main channel, leading to an earlier cease of salt precipitation in these pores, and thus less aggregated salt particles.

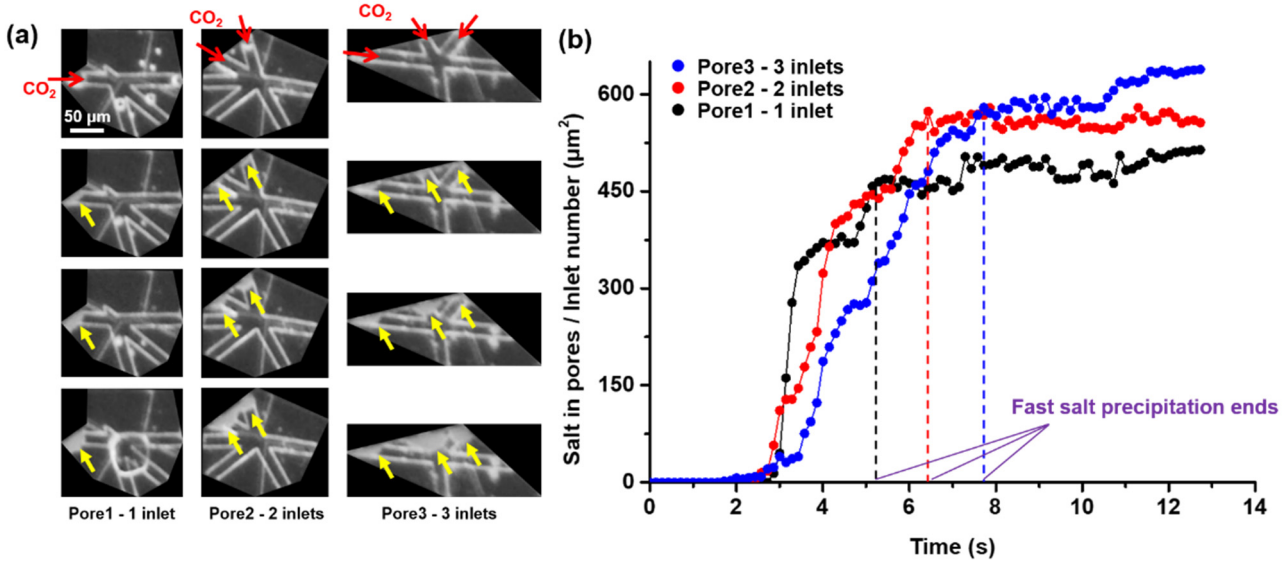

Figure 5. Salt precipitation and accumulation in the 5-μm deep pores. (**a**) Recorded salt precipitation and accumulation results in three individual pores with 1–3 inlets. (**b**) Salt particle accumulation dynamics in three pores.

Previous theoretical study of salt precipitation in porous media indicates that the capillarity drives the water flowing towards the evaporation front, leading to salt accumulation at the outlet of the porous media [11]. Similarly, in a previous experimental study, researchers found that after drying the core initially saturated with brine, precipitated salt is mainly found on the core surface [41]. In our case, when CO_2 is injected into the 5-μm deep pore through the nanochannel, the relatively large pore serves as an open space for water to evaporate and salt to accumulate.

To further analyze the salt accumulation dynamics in pores, we performed the phase-field simulation [42] to evaluate the gas chamber in the pore during CO_2 injection, as shown in Figure 6a. The 2D simulation captures the governing dimension (depth) of the channel (500 nm) and pore (5 μm). We set the pore length as 100 μm, which is the magnitude of the

equivalent diameter of the pore on the chip surface. In the simulation, there is also a 500-nm outlet nanochannel for the solution to be displaced, which is not plotted in Figure 6a. We chose the fluid properties, including viscosity, density and interfacial tension of CO_2 and salt solution at 70 °C and 1 MPa, and set the CO_2 injection pressure as 1 MPa. It is noted that during the experiment, we can only observe the salt precipitation from the top side of the nanofluidic chip. The simulation applies the geometry of the governing dimension (depth). We only used simulation results for qualitative analysis instead of quantitative comparison.

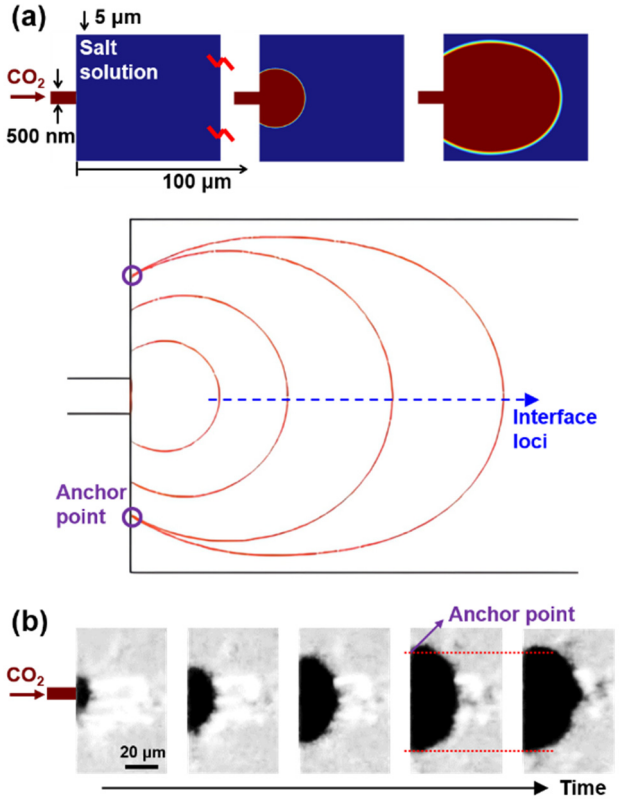

Figure 6. (**a**) Simulation of CO_2 displacing salt solution at the connection between a 500-nm channel and a 5-μm pore. The loci of the CO_2-water interface are plotted by combing multiple frames of simulation results. (**b**) Experimental results of precipitated salt accumulating at a pore inlet. The precipitated salt is colored black for clarity.

The CO_2 displacing salt solution produces a growing gas chamber, as shown in Figure 6a. At the CO_2-water interface, water evaporation causes salt precipitation and accumulation. As the CO_2 displacement front remains curved, the salt precipitation front also grows in a curved shape and accumulates in a sector area (Figures 5a and 7b). In the simulation, the effect of accumulated salt particles on the CO_2 displacing salt solution is not considered. Therefore, the center of the CO_2-water interface moves the fastest during the CO_2 injection (Figure 6a), leading to a center-stretched arc profile. However, in the experiment, we found that the salt accumulation rate at the center is lower than what we expected from the simulation (Figure 6b). The salt accumulation front is actually a center-compressed arc profile. Therefore, the accumulated salt particles at the pore inlet impede CO_2 flow rate severely. In addition, the simulation results indicate that an anchor point of the interface exists during the CO_2 displacing salt solution (Figure 6a). In the experiment, the anchor point is also identified during the salt accumulation, further proving that salt precipitation in pores mainly happens at the CO_2-solution interface with CO_2 injection.

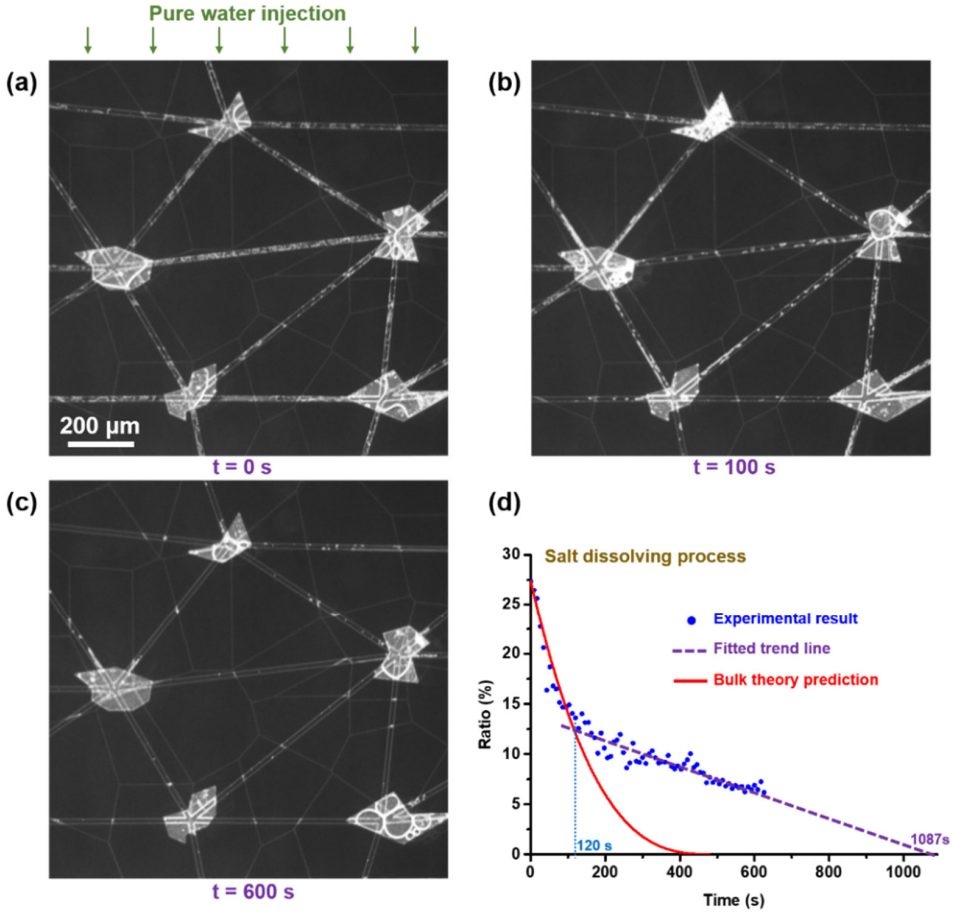

Figure 7. Salt dissolution dynamics in the 500-nm deep network. (**a**–**c**) are recorded images of salt dissolution at 0, 100 and 600 s. (**d**) Experimental results of the salt dissolution process, classical bulk dissolution theory prediction and fitted trend line based on experimental results.

3.3. Salt Dissolution in the Nanoporous Media

We injected pure water into the salt-contaminated chip to study the salt dissolution dynamics in the nanoporous media (Figure 7). The water injection is at constant pressure (1 MPa), and water slowly dissolves salt particles in the 500-nm deep network. The salt precipitation process takes ~13 s during the CO_2 injection, but salt dissolution needs more than 600 s at the same injection pressure (1 MPa). After injecting water for 625.7 s, the occupancy of the solid salt particles in the 500-nm deep network reduces from an initial 27.3% to 6.2%. In the experiment, we did not record long enough to capture the moment when all salt particles get dissolved because of the limited camera memory. We estimated the time needed for salt dissolution in the 500-nm deep network to be ~1087 s by linearly fitting the slow dissolution stage (Figure 7d). The duration of salt dissolution is 83.6 times longer than the duration of salt precipitation. At 70 °C and 1 MPa, the water viscosity is 23.5 times larger than the CO_2 viscosity. Therefore, the water flow rate in the 500-nm deep network is much lower than the CO_2 flow rate. The difference in flow rate contributes to the discrepancy in the time required for salt precipitation and dissolution. The remaining discrepancy (~3.6 times) should be caused by different governing mechanisms of salt precipitation (governed by salt nucleation and water evaporation rate) and dissolution (governed by ion hydration and diffusion).

The salt dissolution dynamics at bulk have been studied early [43], and is characterized by the equation below:

$$V\frac{dw}{dt} = -Kw^{2/3}(w_s - w_0 + w) \tag{11}$$

where V is the volume of solution, w is the weight of salt crystal at time t, K is a positive constant relating to dissolution rate, w_s is the weight of salt needed to saturate liquid phase under given conditions, w_0 is the weight of salt crystal at the beginning. In our case, the pure water is continuously injected. We can assume the salt concentration in the solution is small, and its change is negligible. The Equation (11) can be further simplified as [43]:

$$V\frac{dw}{dt} = -K_1 w^{2/3} \tag{12}$$

where K_1 is also a positive constant relating to dissolution rate, and is different from K. The integration of Equation (12) with the initial condition ($t = 0$, $w = w_0$) gives the expression of salt crystal weight changing with time:

$$w = \left(w_0^{1/3} - \frac{K_1 t}{3}\right)^3 \tag{13}$$

In our experiment, the weight of salt crystal is equivalent as the occupancy of the solid salt particles in the 500-nm deep network. Based on Equation (13), the salt dissolution dynamics is described as:

$$R = \left(R_0^{1/3} - K_2 t\right)^3 \tag{14}$$

where K_2 is also a positive constant relating to dissolution rate, and is different from K and K_1. By fitting the K_2 with our experimental results, we found the classical dissolution theory at bulk only predicts the early fast dissolution stage ($t \leq 120$ s) in the nanoporous media, as shown in Figure 7d. The dissolution process in the 500-nm deep network is expected to take twice as long as the duration predicted by the classical theory (~480 s). Therefore, in the nanoporous media, classical bulk dissolution theory could considerably overestimate the actual dissolution rate.

The lower diffusion coefficient of hydrated ions in the nanoporous media potentially causes the slow dissolution stage ($t > 120$ s) found in our experiment. Previous theoretical studies often indicate that molecular diffusivity in confinement varies from its bulk value when the confinement size reduces to serval times of the molecular diameter (i.e., sub-10 nm) [44,45]. Experimental studies find that even at 10^2 nm confinement size, the molecular diffusivity can be reduced significantly. For example, researchers used the conical nanochannel with an orifice radius at 872 nm to measure the diffusivity of the FITC fluorescent dye molecule (molecular diameter at ~2 nm) in confinement. They found that the diffusivity of the FITC molecule reduces from 3.32×10^{-7} cm^2/s in bulk solution to a minimum of 4.61×10^{-8} cm^2/s in confinement [46]. Here the diameters of the hydrated sodium ion and the hydrated chloride ion are ~0.7 nm [47]. The inference is that, for the salt dissolution in the 500-nm network, the initial fast dissolution ($t \leq 120$ s) is governed by the hydration of ions, while the later slow dissolution is governed by the diffusion of hydrated ions at the 500-nm scale. Overall, our experimental findings prove that classical dissolution theory fails to predict the salt dissolution dynamics at the nanometer pore scale. Further theoretical study is needed to model the entire dissolution process in the nanoporous media.

4. Conclusions

In this work, we developed a multiscale shale micromodel (50 nm, 500 nm and 5 μm) to characterize the salt precipitation during CO_2 injection, as well as the salt dissolution during water injection. For the salt precipitation in the nanoporous media, we found that salt precipitation mainly happens in the 500-nm deep network. Two stages of salt precipitation (fast and slow) are observed. The precipitation rate ratio of the two stages is ~7.9 times larger than the ratio measured in the microporous media. The slow water evaporation and fast heterogeneous nucleation in nanoporous media potentially contribute to the difference in the precipitation rate ratio in nanoporous and microporous media.

In addition to the nanometer pore network, salt precipitation also happens at the connection between the 500-nm deep network and 5-μm deep pores. Salt particles accumulate in a sector region that aligns with the CO_2 displacement front. During the water injection, the salt dissolution in the 500-nm network takes approximately twice as long as the prediction from the classical bulk dissolution theory. The theory only predicts the initial fast dissolution in the experiment, but misses the later slow dissolution stage, indicating the failure of bulk theory at the nanoscale.

Overall, this work provides nanometer pore-scale insight into salt precipitation and dissolution during CO_2 and water injection. The experimental findings shed light on CO_2 injection for shale oil recovery when high salinity water exists. We conducted preliminary theoretical analyses of experimental results. Further theoretical modeling work to dig into the fundamental mechanisms of salt precipitation and dissolution dynamics at the nanoscale is urgently needed. In addition, the injected CO_2 is often at the supercritical condition in shale reservoirs. Characterizing the effect of supercritical CO_2 on salt precipitation is also required.

Author Contributions: Software, H.D.; Investigation, X.H.; Resources, X.H., H.X. and L.Z. (Lei Zhang); Data curation, L.Z. (Liang Zhang) and W.S.; Writing—review & editing, H.S.; Visualization, Z.W.; Supervision, J.Y. and J.Z.; Project administration, J.Z.; Funding acquisition, J.W. and J.Z. All authors have read and agreed to the published version of the manuscript.

Funding: The authors gratefully acknowledge the generous support from the National Natural Science Foundation of China (No. 52174051), Excellent Young Scholars of Shandong Province (No. 2022HWYQ-072), Guanghua Scholars of China University of Petroleum (East China) (No. 20210002) as well as research fund provided by the Exploration and Development Research Institute Sinopec Jianghan Oilfield Company.

Conflicts of Interest: The authors declare no conflict of interest.

References

1. Jia, B.; Tsau, J.-S.; Barati, R. A review of the current progress of CO_2 injection EOR and carbon storage in shale oil reservoirs. *Fuel* **2019**, *236*, 404–427.
2. Mukhina, E.; Cheremisin, A.; Khakimova, L.; Garipova, A.; Dvoretskaya, E.; Zvada, M.; Kalacheva, D.; Prochukhan, K.; Kasyanenko, A.; Cheremisin, A. Enhanced Oil Recovery Method Selection for Shale Oil Based on Numerical Simulations. *ACS Omega* **2021**, *6*, 23731–23741. [CrossRef] [PubMed]
3. Burrows, L.C.; Haeri, F.; Cvetic, P.; Sanguinito, S.; Shi, F.; Tapriyal, D.; Goodman, A.; Enick, R.M. A Literature Review of CO_2, Natural Gas, and Water-Based Fluids for Enhanced Oil Recovery in Unconventional Reservoirs. *Energy Fuels* **2020**, *34*, 5331–5380. [CrossRef]
4. Feng, Q.; Xu, S.; Xing, X.; Zhang, W.; Wang, S. Advances and challenges in shale oil development: A critical review. *Adv. Geo-Energy Res.* **2020**, *4*, 406–418. [CrossRef]
5. Wu, W.; Zoback, M.D.; Kohli, A.H. The impacts of effective stress and CO_2 sorption on the matrix permeability of shale reservoir rocks. *Fuel* **2017**, *203*, 179–186. [CrossRef]
6. Alfarge, D.; Wei, M.; Bai, B. Factors Affecting CO_2-EOR in Shale-Oil Reservoirs: Numerical Simulation Study and Pilot Tests. *Energy Fuels* **2017**, *31*, 8462–8480. [CrossRef]
7. Yu, H.; Xu, H.; Fu, W.; Lu, X.; Chen, Z.; Qi, S.; Wang, Y.; Yang, W.; Lu, J. Extraction of shale oil with supercritical CO_2: Effects of number of fractures and injection pressure. *Fuel* **2021**, *285*, 118977. [CrossRef]
8. Khan, H.J.; Spielman-Sun, E.; Jew, A.D.; Bargar, J.; Kovscek, A.; Druhan, J.L. A Critical Review of the Physicochemical Impacts of Water Chemistry on Shale in Hydraulic Fracturing Systems. *Environ. Sci. Technol.* **2021**, *55*, 1377–1394. [CrossRef]
9. Zhang, Y.; Ju, B.; Zhang, M.; Wang, C.; Zeng, F.; Hu, R.; Yang, L. The effect of salt precipitation on the petrophysical properties and the adsorption capacity of shale matrix based on the porous structure reconstruction. *Fuel* **2022**, *310*, 122287.
10. Fakher, S.; Imqam, A. Asphaltene precipitation and deposition during CO_2 injection in nano shale pore structure and its impact on oil recovery. *Fuel* **2019**, *237*, 1029–1039. [CrossRef]
11. Miri, R.; Hellevang, H. Salt precipitation during CO_2 storage—A review. *Int. J. Greenh. Gas Control* **2016**, *51*, 136–147. [CrossRef]
12. Kumar, S.; Foroozesh, J.; Edlmann, K.; Rezk, M.G.; Lim, C.Y. A comprehensive review of value-added CO_2 sequestration in subsurface saline aquifers. *J. Nat. Gas Sci. Eng.* **2020**, *81*, 103437. [CrossRef]
13. Lebedev, M.; Zhang, Y.; Sarmadivaleh, M.; Barifcani, A.; Al-Khdheeawi, E.; Iglauer, S. Carbon geosequestration in limestone: Pore-scale dissolution and geomechanical weakening. *Int. J. Greenh. Gas Control* **2017**, *66*, 106–119. [CrossRef]
14. De Silva, P.N.K.; Ranjith, P.G. A study of methodologies for CO_2 storage capacity estimation of saline aquifers. *Fuel* **2012**, *93*, 13–27. [CrossRef]

15. Peysson, Y.; André, L.; Azaroual, M. Well injectivity during CO_2 storage operations in deep saline aquifers—Part 1: Experimental investigation of drying effects, salt precipitation and capillary forces. *Int. J. Greenh. Gas Control* **2014**, *22*, 291–300. [CrossRef]
16. Ott, H.; Snippe, J.; de Kloe, K. Salt precipitation due to supercritical gas injection: II. Capillary transport in multi porosity rocks. *Int. J. Greenh. Gas Control* **2021**, *105*, 103233. [CrossRef]
17. Oh, J.; Kim, K.-Y.; Han, W.S.; Kim, T.; Kim, J.-C.; Park, E. Experimental and numerical study on supercritical CO_2/brine transport in a fractured rock: Implications of mass transfer, capillary pressure and storage capacity. *Adv. Water Resour.* **2013**, *62*, 442–453. [CrossRef]
18. Kim, K.-Y.; Han, W.S.; Oh, J.; Kim, T.; Kim, J.-C. Characteristics of Salt-Precipitation and the Associated Pressure Build-Up during CO_2 Storage in Saline Aquifers. *Transp. Porous Media* **2012**, *92*, 397–418. [CrossRef]
19. Alhamad, L.; Miskimins, J. Minimizing calcium lactate precipitation via the addition of gluconate ions for matrix acidizing with lactic acid. *J. Pet. Sci. Eng.* **2022**, *218*, 110995. [CrossRef]
20. Wang, H.; Liu, W. Research on numerical simulation method of salt dissolution and recrystallization of inter-salt shale oil reservoir. *J. Pet. Sci. Eng.* **2022**, *213*, 110464. [CrossRef]
21. Zhang, D.; Kang, Y.; Selvadurai, A.P.S.; You, L. Experimental Investigation of the Effect of Salt Precipitation on the Physical and Mechanical Properties of a Tight Sandstone. *Rock Mech. Rock Eng.* **2020**, *53*, 4367–4380. [CrossRef]
22. Zhang, Y.; Zhang, M.; Mei, H.; Zeng, F. Study on salt precipitation induced by formation brine flow and its effect on a high-salinity tight gas reservoir. *J. Pet. Sci. Eng.* **2019**, *183*, 106384. [CrossRef]
23. Shao, J.; You, L.; Kang, Y.; Chen, M. Experimental investigation of effect of salt crystallization on the mechanical strength of shale. *J. Pet. Sci. Eng.* **2022**, *213*, 110366. [CrossRef]
24. Kim, M.; Sell, A.; Sinton, D. Aquifer-on-a-Chip: Understanding pore-scale salt precipitation dynamics during CO_2 sequestration. *Lab Chip* **2013**, *13*, 2508–2518. [CrossRef] [PubMed]
25. He, D.; Jiang, P.; Xu, R. Pore-Scale Experimental Investigation of the Effect of Supercritical CO_2 Injection Rate and Surface Wettability on Salt Precipitation. *Environ. Sci. Technol.* **2019**, *53*, 14744–14751. [CrossRef]
26. Zhong, J.; Riordon, J.; Zandavi, S.H.; Xu, Y.; Persad, A.H.; Mostowfi, F.; Sinton, D. Capillary Condensation in 8 nm Deep Channels. *J. Phys. Chem. Lett.* **2018**, *9*, 497–503. [CrossRef]
27. Yang, Q.; Jin, B.; Banerjee, D.; Nasrabadi, H. Direct visualization and molecular simulation of dewpoint pressure of a confined fluid in sub-10 nm slit pores. *Fuel* **2019**, *235*, 1216–1223. [CrossRef]
28. Zhong, J.; Alibakhshi, M.A.; Xie, Q.; Riordon, J.; Xu, Y.; Duan, C.; Sinton, D. Exploring Anomalous Fluid Behavior at the Nanoscale: Direct Visualization and Quantification via Nanofluidic Devices. *Acc. Chem. Res.* **2020**, *53*, 347–357. [CrossRef]
29. Xie, Q.; Alibakhshi, M.A.; Jiao, S.; Xu, Z.; Hempel, M.; Kong, J.; Park, H.G.; Duan, C. Fast water transport in graphene nanofluidic channels. *Nat. Nanotechnol.* **2018**, *13*, 238–245. [CrossRef]
30. Wang, L.; Boutilier, M.S.; Kidambi, P.R.; Jang, D.; Hadjiconstantinou, N.G.; Karnik, R. Fundamental transport mechanisms, fabrication and potential applications of nanoporous atomically thin membranes. *Nat. Nanotechnol.* **2017**, *12*, 509. [CrossRef]
31. Zhong, J.; Abedini, A.; Xu, L.; Xu, Y.; Qi, Z.; Mostowfi, F.; Sinton, D. Nanomodel visualization of fluid injections in tight formations. *Nanoscale* **2018**, *10*, 21994–22002. [CrossRef] [PubMed]
32. Zhong, J.; Zhao, Y.; Lu, C.; Xu, Y.; Jin, Z.; Mostowfi, F.; Sinton, D. Nanoscale Phase Measurement for the Shale Challenge: Multicomponent Fluids in Multiscale Volumes. *Langmuir* **2018**, *34*, 9927–9935. [CrossRef] [PubMed]
33. Jatukaran, A.; Zhong, J.; Persad, A.H.; Xu, Y.; Mostowfi, F.; Sinton, D. Direct Visualization of Evaporation in a Two-Dimensional Nanoporous Model for Unconventional Natural Gas. *ACS Appl. Nano Mater.* **2018**, *1*, 1332–1338. [CrossRef]
34. Ho, T.-H.M.; Tsai, P.A. Microfluidic salt precipitation: Implications for geological CO_2 storage. *Lab Chip* **2020**, *20*, 3806–3814. [CrossRef] [PubMed]
35. Gruener, S.; Huber, P. Knudsen Diffusion in Silicon Nanochannels. *Phys. Rev. Lett.* **2008**, *100*, 064502. [CrossRef] [PubMed]
36. Persad, A.H.; Ward, C.A. Expressions for the Evaporation and Condensation Coefficients in the Hertz-Knudsen Relation. *Chem. Rev.* **2016**, *116*, 7727–7767. [CrossRef]
37. Khaleghi, A.; Sadrameli, S.M.; Manteghian, M. Thermodynamic and kinetics investigation of homogeneous and heterogeneous nucleation. *Rev. Inorg. Chem.* **2020**, *40*, 167–192. [CrossRef]
38. Gebauer, D.; Raiteri, P.; Gale, J.D.; Cölfen, H. On classical and non-classical views on nucleation. *Am. J. Sci.* **2018**, *318*, 969–988. [CrossRef]
39. Zimmermann, N.E.R.; Vorselaars, B.; Quigley, D.; Peters, B. Nucleation of NaCl from Aqueous Solution: Critical Sizes, Ion-Attachment Kinetics, and Rates. *J. Am. Chem. Soc.* **2015**, *137*, 13352–13361. [CrossRef]
40. Nakamuro, T.; Sakakibara, M.; Nada, H.; Harano, K.; Nakamura, E. Capturing the Moment of Emergence of Crystal Nucleus from Disorder. *J. Am. Chem. Soc.* **2021**, *143*, 1763–1767. [CrossRef]
41. Desarnaud, J.; Derluyn, H.; Molari, L.; de Miranda, S.; Cnudde, V.; Shahidzadeh, N. Drying of salt contaminated porous media: Effect of primary and secondary nucleation. *J. Appl. Phys.* **2015**, *118*, 114901. [CrossRef]
42. Guangpu, Z.; Aifen, L. Interfacial dynamics with soluble surfactants: A phase-field two-phase flow model with variable densities. *Adv. Geo-Energy Res.* **2020**, *4*, 86–98.
43. Noyes, A.A.; Whitney, W.R. The rate of solution of solid substances in their own solutions. *J. Am. Chem. Soc.* **1897**, *19*, 930–934. [CrossRef]

44. Wang, H.; Wang, X.; Jin, X.; Cao, D. Molecular Dynamics Simulation of Diffusion of Shale Oils in Montmorillonite. *J. Phys. Chem. C* **2016**, *120*, 8986–8991. [CrossRef]
45. Zhang, W.; Feng, Q.; Wang, S.; Xing, X. Oil diffusion in shale nanopores: Insight of molecular dynamics simulation. *J. Mol. Liq.* **2019**, *290*, 111183. [CrossRef]
46. Zhang, L.-X.; Cao, X.-H.; Cai, W.-P.; Li, Y.-Q. Observations of the Effect of Confined Space on Fluorescence and Diffusion Properties of Molecules in Single Conical Nanopore Channels. *J. Fluoresc.* **2011**, *21*, 1865–1870. [CrossRef]
47. Tansel, B.; Sager, J.; Rector, T.; Garland, J.; Strayer, R.F.; Levine, L.; Roberts, M.; Hummerick, M.; Bauer, J. Significance of hydrated radius and hydration shells on ionic permeability during nanofiltration in dead end and cross flow modes. *Sep. Purif. Technol.* **2006**, *51*, 40–47. [CrossRef]